

Heterogeneous Microstructure and Corrosion Resistance of the EH36 Steel Joined by Vertical Electro-Gas Welding

Jianglong Yi^{1,*}, Ben Niu¹, Wenwen Gao¹, Yaoyong Yi¹, Yu Wang^{1,2}, Chen Yu¹, Dan Liu¹, Kai Wang², Zexin Jiang³, Jinjun Ma³

¹ Guangdong Provincial Key Laboratory of Advanced Welding Technology, Guangdong Welding Institute (China-Ukraine E. O. Paton Institute of Welding), Guangzhou, 510650, PR China

² Foshan University, Foshan, Guangdong, 528000, PR China

³ Guangzhou Shipyard International Co., Ltd., Guangzhou, China

*E-mail: Yijl@gwi.gd.cn

Received: 14 November 2019 / Accepted: 12 December 2019 / Published: 10 February 2020

This study aimed to systematically investigate the heterogeneous microstructures and corrosion resistance of the EH36 welded joint fabricated through vertical electro-gas welding (VEGW) at a high heat input (about 308 kJ/cm). In addition to the conventional electrochemical measurement techniques, the scanning vibrating electrode technique (SVET) was also employed to examine the localized corrosion behavior of the welded joint. Our results suggested that, the welded joint consisted of four different distinguishable microstructures, which were the coarse-grain heat affected zones, fine-grain heat affected zones, incomplete heat affected zone and weld metal zones. Meanwhile, these different zones were easily distinguished in the SVET map. Besides, the WM showed positive corrosion resistance compared with the other regions, except in the root layer. The highest R_{ct} value (226.6 $\Omega \cdot \text{cm}^2$) was obtained in WM of the top layer, and the most negative corrosion resistance appeared in BM of the middle layer. Additionally, results of SVET current density distribution map, microhardness and Charpy impact test also confirmed the varying tendency of the heterogeneous microstructures of the welded joint. Finally, it was discovered that the corrosion resistance in various regions of this VEGW joint was determined by its microstructure and chemical composition.

Keyword: Vertical electro-gas welding; Heterogeneous microstructures; Corrosion; SVET

1. INTRODUCTION

The EH36 grade high-intensity structural steel has been widely used in the fields of marine and offshore platforms, especially for those with heavy structural construction that serve in harsh environment, which can be ascribed to its high strength, good low temperature impact toughness, and excellent weldability [1]. To enhance the productivity of those heavy structures, some single-pass

welding technologies with high weld heat input, such as vertical electrogas welding (VEGW), flux copper backing welding (FCB), and electroslag welding (ESW), have been extensively utilized to replace the traditional multi-pass welding process [2].

Barbosa et al. [3] noticed that, the reduced number of welding passes often brought high heat input, which potentially resulted in the formation of solidification structure with large spacing, giving rise to the formation of a heterogeneous and thicker microstructure that finally prejudiced the mechanical performance of the weld metal. The above microstructure discontinuities of welded joint can be reduced through using the suitable filler metal and welding process. However, such heterogeneous microstructures of welded joint can not be eliminated due to its nature characteristic together with different resistance to corrosion. Pimenta et al. [4] found that, the weld metal remained prone to corrosion even though the most advanced welding technology, such as laser and electron beam welding, was used. According to Liu et al. [5], the welding process accelerated the corrosion behavior of the high-strength low alloy steel. Such phenomenon is not only related to the metallurgical changes, but also to the various residual stresses distributed in the fusion zone and the heat affected zone.

Over the past decade, tremendous studies have been carried out to explore the relationship of the microstructure with the mechanical properties of the HSLA welded joint. Nonetheless, seldom studies have focused on investigating the correlation of microstructure with the corrosion behavior of weld metal. Deen et al. [6] proved that, the presence of acicular ferrite structure in the weld zone of low alloy steel weldment deteriorated the corrosion resistance in aerated water and NaCl solution. Compared with allotriomorphic and widmanstätten ferrite, the needle-like acicular ferrite is prone to form the non-uniform oxide, which restricts the subsequent formation of complete coverage oxide film on the weld zone surface. Fattahi et al. [7] confirmed that the corrosion resistance of the weld metal decreased as the Ti-based inclusions and acicular ferrite in the microstructure increased. Such finding may not only be attributed to the presence of the non-metallic Ti-based inclusions that act as the suitable pitting corrosion sites, but also to the increased grain boundaries of the refined acicular ferrite.

In this study, we attempted to find the correlation of heterogeneous microstructures with the corrosion resistance of the EH36 steel welded joint. To this aim, vertical electro-gas welding (VEGW), a single-pass weld with less microstructural complexity, was adopted to fabricate the EH36 high-strength steel weld metal. In addition, metallographic microscopy and scanning electron microscopy (SEM) were carried out to illuminate the microstructural evolution of the welded joint in different regions. Meanwhile, the scanning vibrating electrode technique (SVET) was also employed to assess the localized corrosion behavior of the welded joint. Typically, SVET is a unique “visualizing” electrochemical test method, which provides the current density picture of the metal surface under the whole corrosion processes, as suggested by Bastos et al. [8] Under the assistance of other electrochemical test techniques and modeling tools, the corrosion behavior was quantitatively investigated. Hence, the relationship between the complex corrosion resistance of the EH36 steel welded joint and its heterogeneous microstructures was examined in this study by the use of this new local electrochemical test technique. Our findings would provide certain guidance for the suitable VEGW welding process.

2. MATERIAL AND EXPERIMENTAL PROCEDURE

2.1 Material and welding procedure

Two ship steel EH36 plates with a dimension of 300mm×150mm×40mm were used to fabricate the VEGW joint. The detailed components and mechanical properties are listed in Table 1 and Table 2, respectively. As shown in Fig.1, the weld groove of the experimental steel formed an angle of 32°, with a gap of 8 mm on the bottom. The schematic diagram of the welding process is described in Fig.2. The SC-EG3 wire that was 1.6 mm in diameter was used as the VEGW filler metal. The chemical compositions of the welded metal are also listed in Table 1. Notably, the suitable welding parameters for this welding experiment were set below, welding current of 400 A, welding voltage of 40 V, welding speed of 31.2 mm/min, and heat input of 308 KJ/cm. In addition, the purified carbon dioxide was used as the shielding gas at a rate of 16 L/min.

Table 1. Chemical compositions of the base metal and the welded metal

Material	C	Si	Mn	Ni	Mo	Cr	V	Cu	P	S	Fe
Base metal	0.08	0.24	1.52	0.33	0.003	0.01	0.033	0.01	0.009	0.001	Bal.
Welded metal	0.12	0.32	1.69	1.28	0.13	0.12	0.04	0.21	0.011	0.008	Bal.

Table 2 Mechanical properties of the EH36 steel

Yield Strength (MPa)	Tensile Strength (MPa)	Elongation rate (%)	Impact Energy (-40°C, J)
438	510	29	240

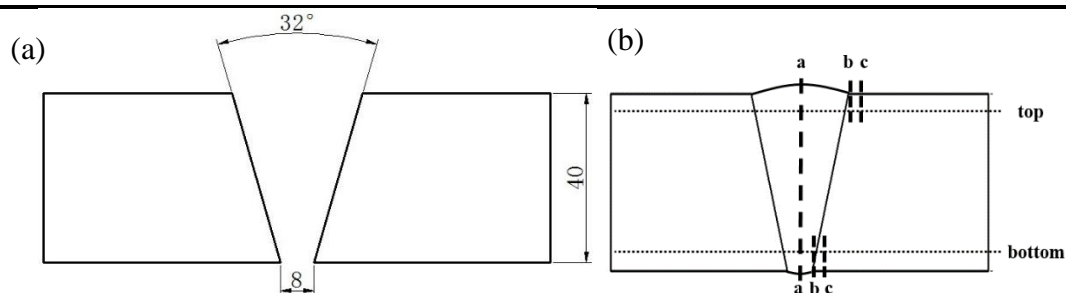


Figure 1 (a) Schematic diagram of the welded groove and (b) Cut mode of the impact test: a. the center of the weld metal; b. fusion line; c. 2 mm to the fusion line in the heat affected zone

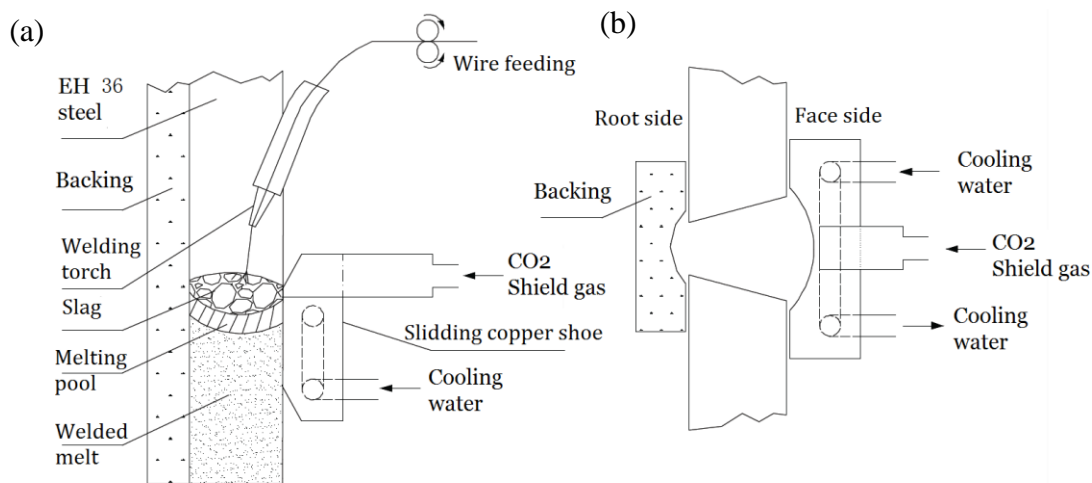


Figure 2 Schematic diagram of the welding process (a) Cross-section view; (b) Vertical view

2.2 Microstructure analysis

It is well known that, a single-pass welding technique with high weld heat input can generate heterogeneous structures not only in HAZ, but also in the VEGW-welded thick steel plate. Therefore, different zones of weld joint should be carefully observed by means of optical microscope (OM) and SEM.

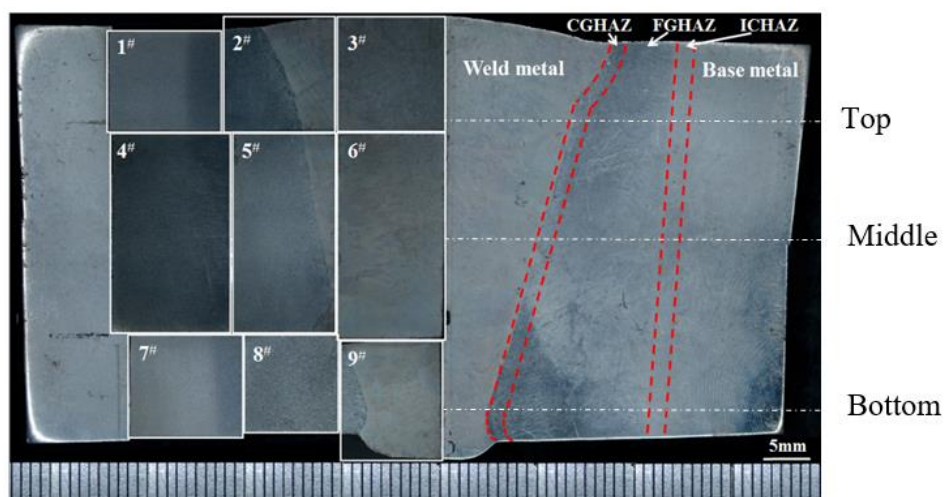


Figure 3 Macrograph of the one-pass EH36 steel weldment (Left: Cut mode for the electrochemical analyses; Right: Schematic diagram of optical microscopic microstructure test)

In this study, the test joint was first obtained by cutting from the longitudinally welded EH36 steel, which contained the base metal (BM), heat affected zone (HAZ) and welded metal (WM), as observed in Fig.3. Moreover, the optical microscopic microstructures of the joints were tested using the DMM-440D optical microscope according to the marks of lines in Fig.3, which started from the

right side to the middle of the joint. Subsequently, small pieces of the test specimens used for electrochemical and microstructure analyses were cut from the left side of the weld joint, also shown in Fig.3, which were marked as 1[#] to 9[#].

2.3 Mechanical and corrosion test

The Vickers microhardness performance on the different surface areas of the weld joint was tested using the DHV-1000Z micro Vickers hardness tester. Three sets of measurements were recorded according to the lines marked as a, b and c in Fig.4a, under a load of 300 g and a dwell time of 10 s. The mechanical properties of the weld joint were examined according to the Germanischer Lloyd standard. The cut mode of the impact test specimens is presented in Fig.1b. Besides, the Charpy impact tests were carried out at -40 °C, and the dimension of the test specimens was 10mm×10mm×50mm.

A special three-electrode electrochemical cell that was designed to expose 1 cm² of the working electrode was utilized for the electrochemical measurements. All specimens, as marked as 1[#] to 9[#], were then mounted on the bottom of this electrochemical cell as the working electrodes, and the center surface was exposed for the electrochemical test. The other two electrodes included a saturated calomel electrode reference electrode and a platinum plate auxiliary electrode, respectively. Prior to tests, the specimens were mechanically polished using the 400, 600, 800 and 2000 grid sandpaper, respectively, then cleaned with distilled water and dried in air. On the other hand, the **open circuit potential** (OCP) and potentiodynamic polarization tests were conducted within the 3.5 wt.% NaCl aqueous solution after 30 min of immersion. Meanwhile, the electrochemical impedance spectroscopy (EIS) and SVET test began after a 30-min immersion within the 3.5 wt.% NaCl aqueous solution. The electrochemical workstation (GAMRY Interface 1010) and the VersaSCAN electrochemical scanning system (AMETEK, VersaSCAN) were thereafter employed to examine the above electrochemical behaviors. Potentiodynamic curves were recorded at the scanning rate of 1 mV/s from -0.3 V to 0.3 V. The EIS measurements were set under the OCP at the frequency of 0.01 Hz~100 KHz, as well as the AC drive signal amplitude of 10 mV. SVET test was performed with the sample dimension of 3mm×3 mm. The Pt-Ir probe was placed above the sample surface, and the height was controlled at between 100 μm-120 μm using a video camera. The SVET measurements were conducted under the OCP, with the vibrating amplitude and vibrating frequency of the micro-probe of 30 μm and 80 Hz, respectively.

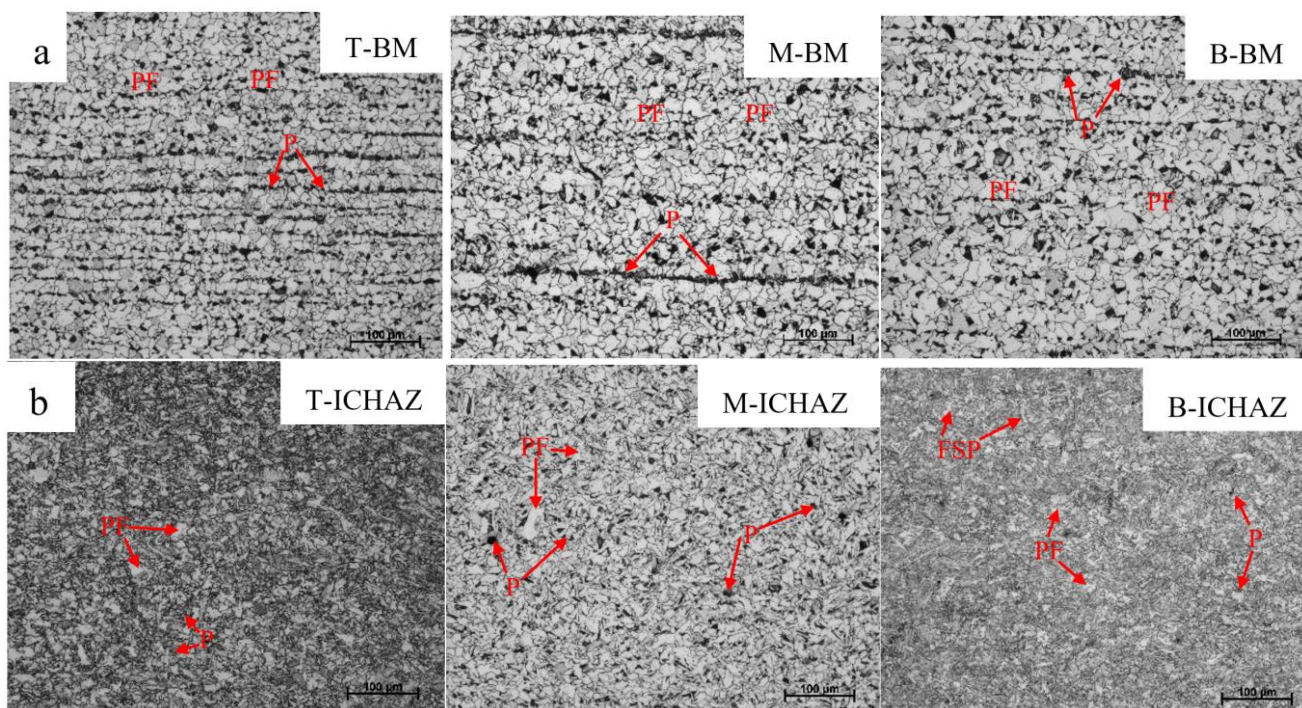
3. RESULTS AND DISCUSSION

3.1 Microstructure

Fig.4 shows the optical microscopic microstructure in different regions of the VEGW samples, which consists of BM, ICHAZ, FGHAZ, CGHAZ, FL and WM in different deposited layers, respectively. Notably, the microstructural heterogeneity was observed not only in the longitudinal direction, but also along the horizontal direction of the joints. According to Fig. 4a, the microstructure of BM was comprised of polygonal ferrite (PF) and pearlite (P) banding, and the pearlite banding was

distributed uniformly along the rolling direction. As the welding heat input increased from the top to the bottom of the joints, the grain size became coarser on the BM bottom. Fig. 4b shows the micrographs of the incomplete heat affected zone (ICHAZ). As was observed, the microstructure of ICHAZ was heterogeneous, especially in terms of the grain types, and the main microstructure was characterized by polygonal ferrite (PF) and pearlite (P). There were more P grains in the middle of the ICHAZ, and the ferrite side plate (FSP) was observed on the ICHAZ bottom. As observed from Fig.4c, the grain size of the FGHAZ was coarser than that of the ICHAZ. As the optical micrograph of the microstructure got closer to the weld metal, the CGHAZ was featured by grain boundary ferrite (GBF), acicular ferrite (AF) and Intragranular ferrite (IF). According to Barbosa et al. [3], such microstructural features was possibly attributed to the complete austenite dissolution and subsequent growth of ferrite grain following heating during the VEGW welding process. Compared with the other welded layers, the middle region showed coarser micro-phase both in FGHAZ and CGHAZ, which was caused by the different heat inputs of the VEGW technology. This phenomenon was also observed based on the widened thickness of CGHAZ adjacent to the fusion line in the middle layer.

The microstructure of WM was composed of polygonal ferrite (PF), granular bainite (GB), ferrite side plate (FSP), martensite (M) and nonmetallic inclusions due to the dissimilar chemical compositions of WM. Moreover, the microstructure in the root WM had a higher volume fraction of AF, which potentially contributed to decreasing the volume fraction of PF and eventually increased the toughness of WM, as suggested by Lee et al. [9]. However, more nonmetallic inclusions were observed in the root WM, which might be resulted from the metallurgical reaction between the ceramic backing and the WM.



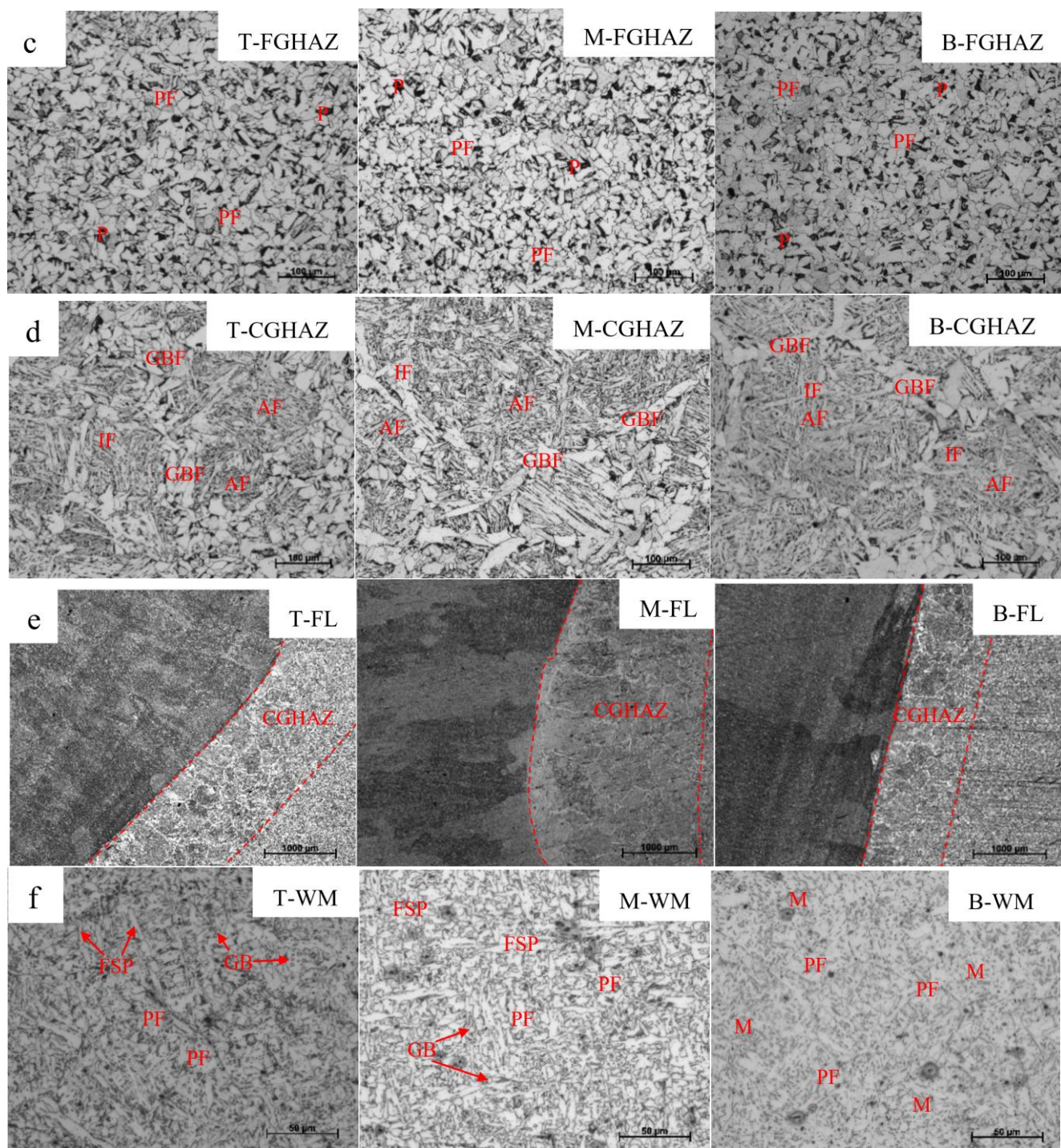


Figure 4. Optical micrographs of different zone. (a) Base Metal, BM; (b) Incomplete heat affected zone, ICHAZ; (c) Fine grained heat-affected zone,FGHAZ;(d) Coarse grained heat-affected zone, CGHAZ; (e) Fuse line, FL; (f) Weld metal, WM of different layers. Note: PF–Polygonal ferrite; P–Pearlite; FSP–Ferrite side plate; AF–Acicular Ferrite; GF–Grain Boundary Ferrite; IF– Intragranular Ferrite; GB–Granular bainite; B–Bainite; M–Martensite

To investigate the detailed microstructural information about the heterogeneity of the welded joint, the specimen SEM micrographs from the fusion line region are presented in Fig 5. Obviously, all WM had more fine grain size than that of HAZ, and the root WM was represented by a mixture of polygonal ferrite and martensite, with a more uniform distribution of inclusion. As shown in Table.3,

the EDS results of the inclusion (marked in Fig.5d) proved that, the inclusions were mainly composed of TiO₂ and CaO. It was reported by Liu et al. [10] that, the inclusions in the steel matrix might cause localized corrosion in the interface region, finally negatively affecting the corrosion resistance of the matrix. Moreover, the EDS results of all samples revealed that there were more Cr, Cu, Ni and Mo elements in the WM than in the HAZ region, among which, the Cr and Cu elements played key roles in improving the corrosion resistance, as reported by Wei et al. [11] and San et al. [12].

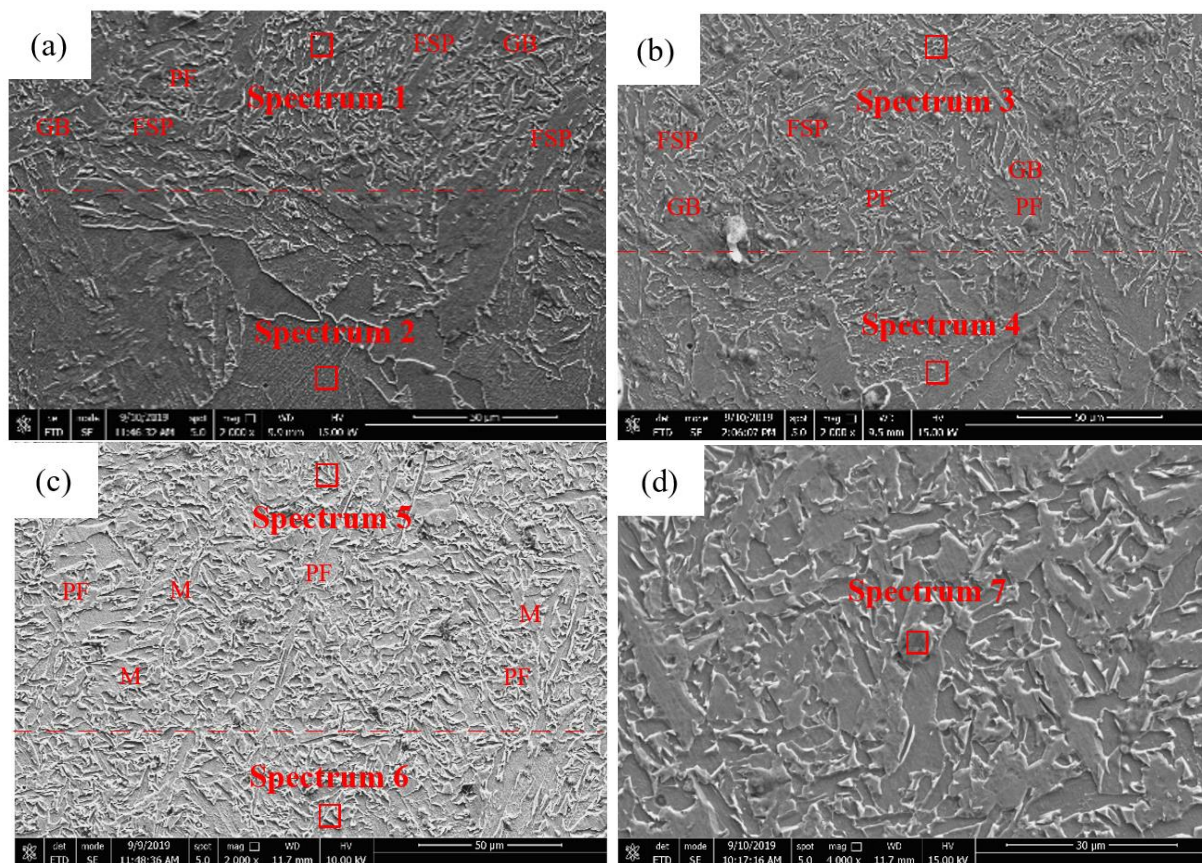


Figure 5 SEM images of the specimen from the fusion line region (The region marked by red rectangle is used for EDS test). (a) the sample 2[#] ; (b) the sample 5[#]; (c) the sample 9[#] ; (d) the inclusion in sample 9[#]

Table 3 Chemical compositions of the EDS point analysis in Fig.5

Element (wt.%)	Fe	Ni	Mn	Cu	Cr	Mo	Ti	Ca	O
Point 1	95.62	1.59	2.36	0.23	0.12	0.08	/	/	/
Point 2	97.27	/	2.27	0.46	/	/	/	/	/
Point 3	95.77	1.55	2.59	0.09	/	/	/	/	/

Point 4	97.8	/	2.20	/	/	/	/	/	/
Point 5	95.4	2.35	2.05	0.06	0.1	0.03	/	/	/
Point 6	97.29	0.44	2.13	0.06	0.06	0.01	/	/	/
Point 7	22.01	/	8.26	/	/	1.68	11.38	8.45	48.21

3.2 Mechanical properties

Fig.6 demonstrates the results of microhardness tests according to the lines marked in the left schematic diagram of the weldment. As was seen, the variation trends of microhardness distribution along lines a, b and c were similar, and the BM and WM showed relatively uniform hardness values. By contrast, the HAZ exhibited obvious fluctuating values. These results were consistent with the varying trend of microstructure. The WM showed the highest hardness values than those in the other regions for all the test deposited layers. The middle-welded layer had the lowest microhardness values, particularly, the values in the BM were obviously lower, which was ascribed to the heat accumulation due to the high weld heat input of VEGW. The microhardness profiles of the middle layer revealed a relatively widened and softened range, which coincided with the widened thickness in M-CGHAZ near the fusion line.

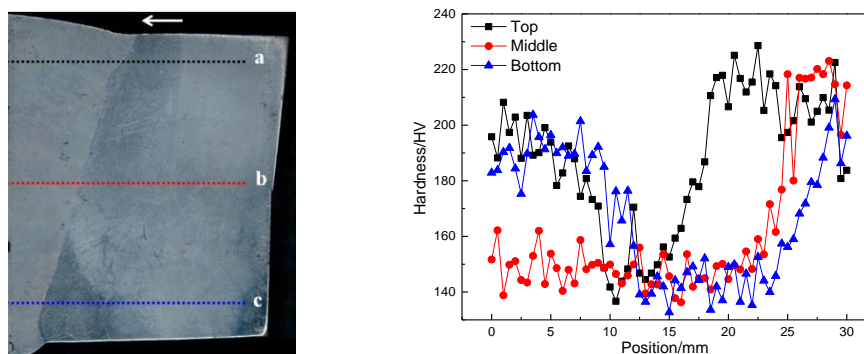


Figure 6 (a) Schematic diagram of the hardness test; (b) Microhardness distribution across the weldment

The toughness of all specimens in the top and bottom layers of the welded joint was examined using the Charpy impact tester. The cut mode is shown in Fig.1b. Table 4 describes the impact absorbed energy results at -40 °C. Clearly, the deteriorating toughness values of the WM specimen were similar among different deposited layers. In addition, the toughness value of the HAZ near the FL was higher than that of FL. For specimens cut from the center of WM in the top and bottom layers, the Charpy impact results were 76.0 J and 85.7 J, respectively. Typically, the increasing toughness in the

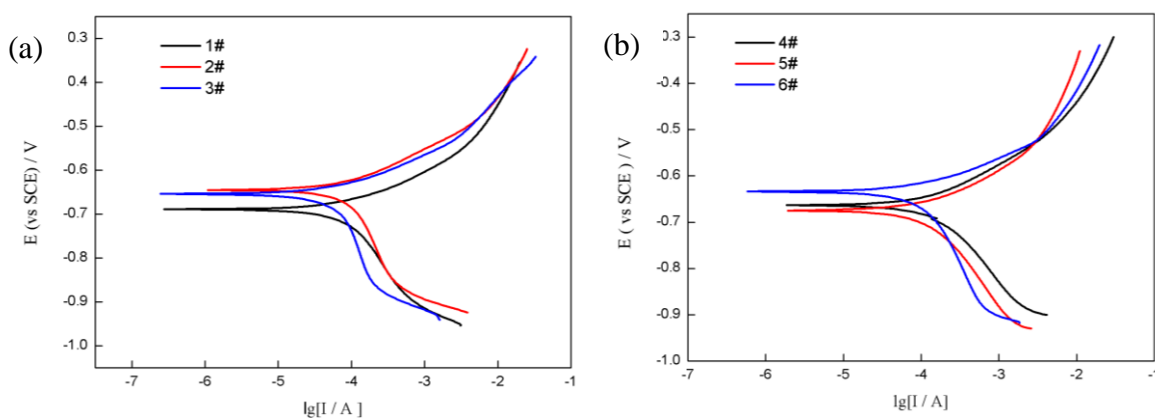
root WM was possibly due to the existence of martensite in the microstructure. This fracture toughness enhancement of martensite was noticed by Earl et al. [13].

Table 4 Results of Charpy impact toughness of VEGW joint

Specimen	Impact Energy (-40°C, J)	Specimen	Impact Energy (-40°C, J)
Center of WM in top layer	76.0	Center of WM in bottom layer	85.7
FL in top layer	141.3	FL in bottom layer	140.0
2mm to the FZ in top of HAZ	219.0	2mm to the FZ in bottom of HAZ	212.7

3.3 Electrochemical behavior

Fig.7 and Fig.8 display the potentiodynamic polarization curves and EIS responses in the different regions of the as-welded VEGW joint within the 3.5% NaCl solution at open circuit potentials, respectively. It was known from the polarization curves shown in Fig. 6 that, all the curves showed similar trends both in cathode and anode behaviors. Besides, the current density increased with the potential during the whole anodic polarization process, indicating no passive film formation on the test sample surface, which also confirmed that the anodic process was controlled by the activation (or charge-transfer) process. On the contrary, the cathodic part of the polarization curve was slightly different from the current, which proved that the cathodic process might be determined by the diffusion-controlled oxygen reduction reaction. As the polarization went on, the oxide layer was formed on the metal surface, which prevented the further oxygen reduction reaction. Deen et al. [6] first showed in their study that, the oxide provided a physical barrier to prohibit the cathodic process. On the other hand, this oxide also played a role as the surface for oxygen reduction instead of the metal base.



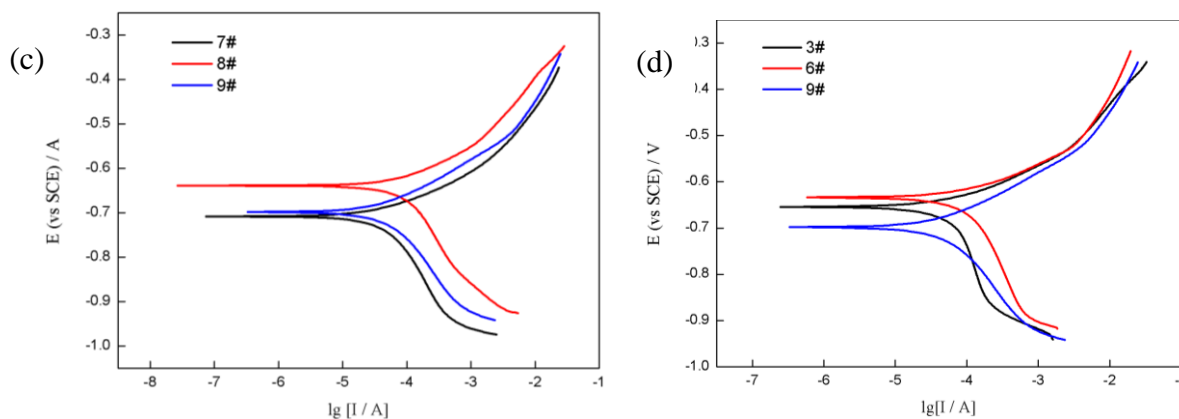


Figure 7. Potentiodynamic polarization curves for different regions of the weldment. (a) Top deposited layer; (b) Middle deposited layer; (c) Bottom deposited layer; (d) WM in different deposited layer

Table 5 lists the electrochemical parameters obtained from the potentiodynamic polarization curves according to the Tafel Curve Fitting method, as reported by McCafferty [14]. Obviously, the heterogenous electrochemical parameters further confirmed the microstructural heterogeneity of this high heat input weldment. It was easily observed that the WM tested in samples 3[#], 6[#] and 9[#] had more positive corrosion potentials than those in other regions, which indicated that the WM showed a higher thermodynamic stability. In the meantime, the corrosion current density of WM was markedly lower than those of HAZ and BM, revealing that the WM exhibited a lower corrosion rate than others in the tested 3.5% NaCl solution. As reported by Qu et al [15], such increased corrosion resistance might contribute to the formation of granular bainite in the welded metal. With regard to the WM regions in different layers, as shown in Fig.6d, the whole potentiodynamic polarization curve showed an obvious tendency along the more negative direction as the deposited layer went from the top to the root weldment. Furthermore, the corrosion current density (I_{corr}) values of the top, middle and bottom layers WM were $5.23 \mu\text{Acm}^{-2}$, $9.22 \mu\text{Acm}^{-2}$ and $4.88 \mu\text{Acm}^{-2}$, respectively, which implied that the WM in the middle layer was prone to quicker corrosion than the others.

Table 5 Potentiodynamic polarization curves parameters of different samples

Different layers	Samples	E_{corr} mV	I_{corr} μAcm^{-2}	β_a (mV/decade)	β_b (mV/decade)
Top	1 [#]	-689	7.29	73	214
	2 [#]	-644	9.35	86	322
	3 [#]	-654	5.23	66	317
	4 [#]	-664	17.2	110	213
Middle	5 [#]	-674	13.6	96	237
	6 [#]	-634	9.22	67	292
	7 [#]	-708	4.21	71	219
Bottom	8 [#]	-639	8.96	90	214
	9 [#]	-698	4.88	90	184

As was observed from the following Nyquist plots present in Fig.8, there was no significant difference among all the tested samples cut from different regions of the EH36 welded joint. Typically, the x-axis and y-axis in the Nyquist plot represented the real impedance (Z_{re}) and imaginary impedance (Z_{im}), respectively. Apparently, a semi-circle was observed in all the plots, which was also indicative of the charge-transfer corrosion process. The diameter of semicircle varied markedly among different regions, not only in the same deposited layer, but also in the same type of area along the longitudinal direction. Notably, the larger diameter of semicircle mainly occurred in the region of WM, which was corresponding to the stronger charge transfer resistance; in addition, the most negative corrosion resistance appeared in the BM of the middle layer. However, some different variations were observed in the Nyquist plot of the bottom layer, which were that, the most negative corrosion resistance appeared in the middle region of HAZ instead of BM, and the WM and BM regions had equal positive corrosion potential values.

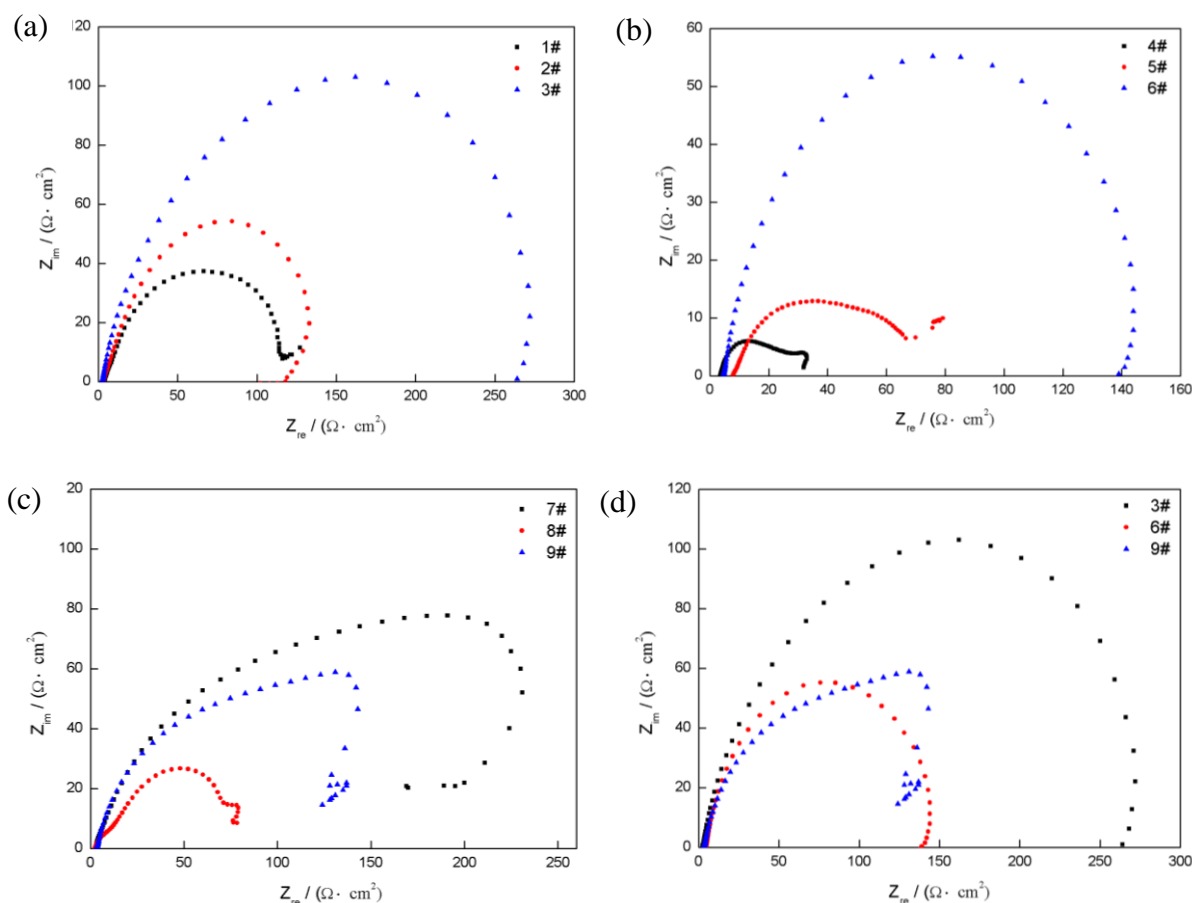


Figure 8 The electrochemical Nyquist plots of different regions of the weldment in 3.5% NaCl solution. (a) Top deposited layer; (b) Middle deposited layer; (c) Bottom deposited layer; (d) WM in different deposited layer

The equivalent circuit and the values of EC elements are depicted in Fig.9 and Table.6, which are obtained according to the Nyquist plot features using the Zimpwin View software. In this

simulated EC model, the impedance of this circuit was in direct proportion to the charge transfer resistance (R_{ct}), which represented the sample corrosion resistance in the electrolyte. Meanwhile, R_s was the solution resistance, which was defined as the formation ability of the oxide film, as reported by Soltis et al. [16].

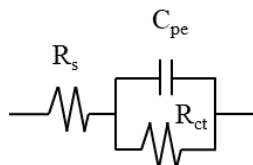


Figure 9. the EC model calculated form the different experimental EIS data

Table 6. Impedance parameters of the EIS tested samples

Different layers	Samples	R_s ($\Omega \cdot \text{cm}^2$)	R_{ct} ($\Omega \cdot \text{cm}^2$)	C (μf)
Top	1 [#]	4.149	107.3	7.591
	2 [#]	3.957	119.0	10.17
	3 [#]	4.420	226.6	8.069
	4 [#]	3.893	39.01	10.65
Middle	5 [#]	9.159	56.15	14.03
	6 [#]	4.965	130.8	21.13
	7 [#]	4.550	183.9	5.456
Bottom	8 [#]	4.226	78.57	7.309
	9 [#]	3.953	129.8	11.95

Clearly, the highest R_{ct} value ($226.6 \Omega \cdot \text{cm}^2$) was obtained on the WM of sample 3[#] in the top deposited layer. Meanwhile, the worst corrosion resistance was detected in the middle layer of the tested sample 4[#]. Overall, the middle layer showed a lower R_{ct} value than those in the other regions, which was consistent with the variation trends of microhardness and potentiodynamic polarization values. As for the different regions of the as-tested samples, R_s showed the same values, except for 5[#] sample, indicating that most of the tested samples exhibited similar trends to form an oxide film. This relatively weak ability to form a dense oxide film in sample 5[#] might be related to its microstructural heterogeneity and the heat accumulation due to the high weld heat input of VEGW.

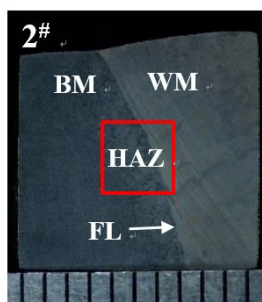
3.4 SVET current density distribution

To clarify the detailed corrosion behavior about the heterogeneous microstructure of the welded EH36 joint, the current density distribution map around the fuse line in different deposited layers of the welded joint was investigated through the SVET method. As shown in Fig.10, all the test areas surrounding the FL in samples 2[#], 5[#], and 9[#] showed obviously heterogeneous local corrosion

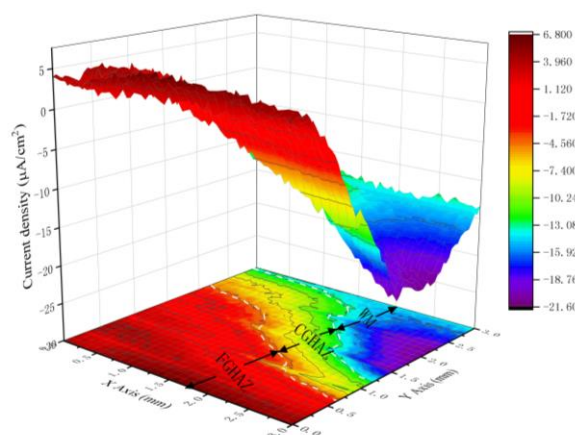
performances. The dissimilar area in the SVET map was easily distinguished, as marked in Fig.10. Interestingly, the SVET current density distribution map exhibited similar characteristics as those of the microstructure. Moreover, different microscopic structures, such as WM, CGHAZ, and FGHAZ, had entirely different current density values, which directly revealed the relationship between the microstructure and the corrosion resistance.

The SVET map of sample 2[#] presented the typical galvanic corrosion features owing to the different micro-area corrosion potentials in WM and BM tested by EIS. The galvanic interaction occurred between the WM and HAZ, in which the anodic and cathodic reactions took place in the FGHAZ and WM, respectively; whereas the CGHAZ was conducted as the transition region from anode to cathode. This heterogeneous corrosion attack was in good agreement with the potentiodynamic polarization test results about the top deposited layer of the VEGW joint. It was concluded that the weld metal in sample 2[#] represented the cathode region, which was protected in this galvanic interaction, while the HAZ region was prone to rapid corrosion in this immersion test. Nonetheless, this galvanic corrosion behavior was not observed in the following SVET maps about samples 5[#] and 9[#]. The SVET probe revealed no cathodic current, and only a total positive current density distribution appeared in Fig.10b and Fig.10d.

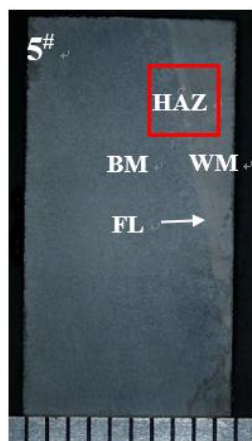
(a)



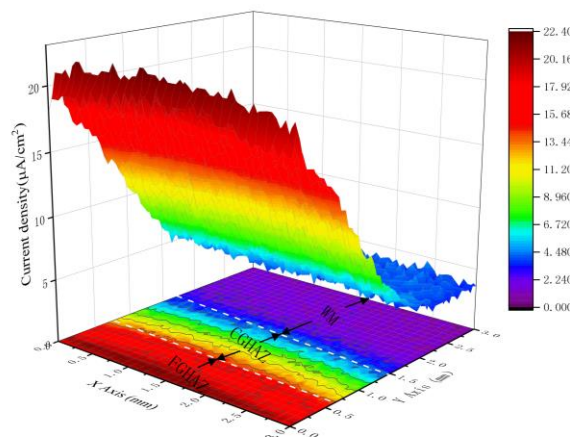
(b)



(c)



(d)



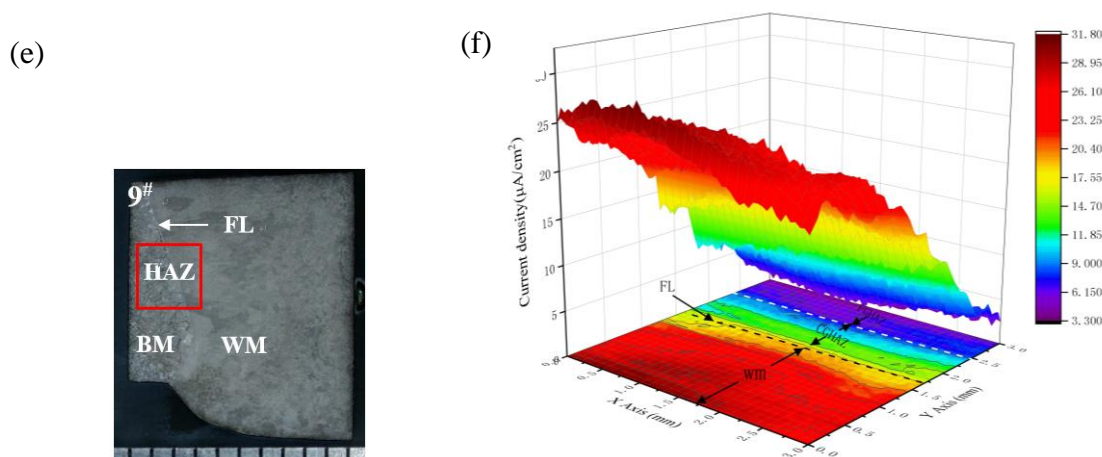


Figure 10 Optical microscopic images and SVET current density distribution mapping of the fusion line regions in different samples. (The region marked by red rectangle is tested by SVET method). (a) Macrograph of the sample 2[#]; (b) SVET map of tested region in sample 2[#]; (c) Macrograph of the sample 5[#] and (d) SVET map of tested region in sample 5[#]; (e) Macrograph of the sample 9[#]; (f) SVET map of tested region in sample 9[#]

This phenomenon might be attributed to the limitations about SVET measurements. According to Ikeuba et al [17] and Paik et al [18], it was difficult to detect the local anodic and cathodic current densities, while the diameter of the Pt-Ir probe tip was larger than the anode-cathode spacing at the active sites. As was observed from Fig.10d, the FGHAZ and CGHAZ of sample 5[#] showed higher current density values than the WM, indicating the worse corrosion performance in the HAZ zones. Apparently, From the top tested sample 2[#] to the root sample 9[#] along the longitudinal direction, the maximum current density gradually increased from $8.5 \mu\text{A}/\text{cm}^2$ to $31.8 \mu\text{A}/\text{cm}^2$. Furthermore, as shown in Fig.10c, the WM of sample 9[#] had the highest current density value (approximately $31.8 \mu\text{A}/\text{cm}^2$) compared with those in other areas, in other words, the corrosion attack first emerged on the root weld metal surface. It was discovered that the root WM had the worst corrosion resistance, on the other hand, the top WM obtained the optimal corrosion properties, which were consistent with the potentiodynamic polarization curves and EIS results.

3.5 Corrosion morphology in different samples

Fig. 11 displays the corrosion morphologies of different specimens with three different fuse line regions after immersion test in the 3.5% NaCl solution for 24 h. According to Fig.11, there was no significant pit corrosion behavior in all the tested samples, and the corrosive products of all samples exhibited a uniform corrosion behavior. Qu et al. [15] and Ha et al. [19] discovered that the corrosion first took place in the ferrite boundary and the interface surrounding the inclusions, and such initial corrosion behavior finally affected the long-term corrosion results. It was apparent that, sample 9[#] demonstrated a loose corrosion product, and samples 2[#] and 5[#] had more compact oxide film covered on the surface, and this surface contributed to preventing the further corrosion, finally improving the anti-corrosive capability.

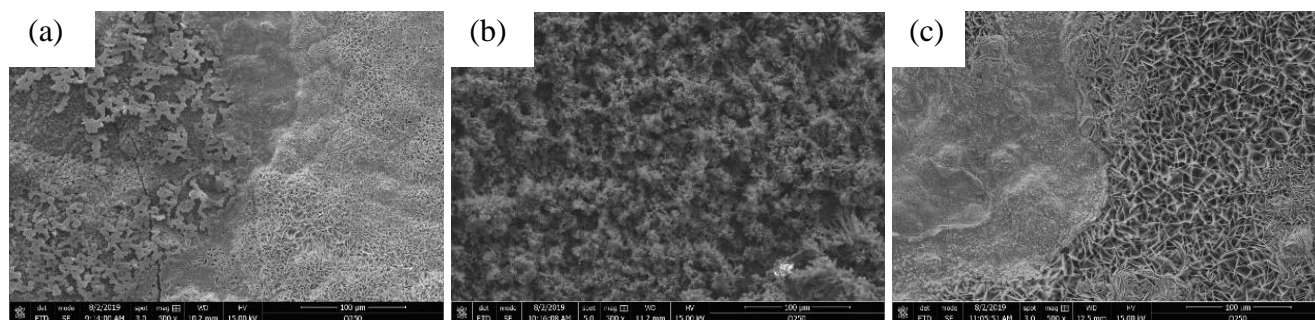


Figure 11 SEM images of the corrosion morphologies after 24 min of immersion in the 3.5% NaCl solution. (a) the sample 2[#] ; (b) the sample 5[#]; (c) the sample 9[#]

4. CONCLUSIONS

In this study, the microstructural heterogeneity features of the VEGW joint are investigated, and the corrosion resistance is also discussed through the conventional electrochemical measurement techniques and the emerging SVET. The major conclusions of this study can be drawn as follows:

(1) The optical microscopic microstructure of the VEGW joint is comprised of different zones, including BM, ICHAZ, FGHAZ, CGHAZ and WM. Microstructural heterogeneity is observed not only in the longitudinal direction, but also long the horizontal direction of the joints. Compared with the other welded layers, the middle region shows coarser micro-phase both in FGHAZ and CGHAZ. Meanwhile, all WM have more fine grain size than that of HAZ, and a uniform distribution of inclusion is observed in the root WM.

(2) Results of microhardness analysis reveal that the middle-welded layer has the lowest microhardness value, which exhibits a relatively broadened and softened range near the fusion line. On the other hand, the Charpy impact value decreases from HAZ to WM; compared with the WM in the top layer, the root WM exhibits superior toughness.

(3) Potentiodynamic polarization and EIS results demonstrate that the WM shows higher positive corrosion resistance than the other regions, with the only exception in the root layer. The highest R_{ct} value ($226.6 \Omega \cdot \text{cm}^2$) is obtained in the WM of the top layer, which is indicative of the best anti-corrosive ability. Overall, the middle layer displays a lower R_{ct} value compared with those in the other regions, and the most negative corrosion resistance appears in the BM of the middle layer.

(4) The SVET results further confirm the microstructural heterogeneity features. With regard to the top layer, a galvanic interaction occurs between the WM and HAZ regions. The weld metal in the top layer acts as the cathode in the galvanic interaction, while the HAZ region is prone to quickly corrode in this immersion test. On the contrary, the corrosion attack first emerges on the root weld metal surface instead of the HAZ region. The inclusions in the root WM matrix may give rise to the localized corrosion in the interface region, eventually deteriorating the corrosion resistance of the matrix.

(5) Moreover, the vertical electro-gas welding (VEGW) technique still causes the formation

of heterogeneous microstructures, which finally generate the heterogenous mechanical and electrochemical properties.

ACKNOWLEDGEMENT

This work was supported by the project of technical project of Guangzhou (201604046026, 201704030112, 201807010035), the project of Inter-Governmental S&T Cooperation (CU03-08), the technical project of Guangdong (20180508, 2017A070701026, 2014B070705007) and the GDAS' Project of Science and Technology Development (2017GDASCX-0113).

References

1. Y.M. Rong, T. Lei, J.J. Xu, Y. Huang, C.M. Wang, *International Journal of Mechanical Sciences*, 146-147 (2018) 180.
2. Y.Q. Zhang, H.Q. Zhang, W.M. Liu, *Journal of Iron and Steel Research International*, 16 (2008) 73.
3. L.H.S. Barbosa, P.J. Modenesi, L.B. Godefroid, A.R. Arias, *International Journal of Fatigue*, 119 (2019) 43.
4. G. Pimenta, T.A. Jarman, The corrosion of metal joints, chapter 3-35, in Shreir's Handbook of Corrosion, 3rd edition (2010) 2447.
5. W. Liu, H. Pan, L. Li, H. Lv, Z. Wu, F. Cao, J. Zhu, *Journal of Manufacturing Processes*, 25 (2017) 418.
6. K.M. Deen, R. Ahmad, I.H. Khan, Z. Farahat, *Materials & Design*, 31 (2010) 3051.
7. M. Fattahi, N. Nabhani, E. Rafiee, M. Nasibi, E. Ahmadi, Y. Fattahi, *Materials Chemistry and Physics*, 146 (2014) 105.
8. A.C. Bastos, M.C. Quevedo, O.V. Karavai, M.G.S. Ferreira, *Journal of The Electrochemical Society*, 164 (2017) C973.
9. J.S. Lee, S.H. Jeong, D.Y. Lim, J.O. Yun, M.H. Kim, *Metals and Materials International*, 16 (2010) 827.
10. C. Liu, R.I. Revilla, D.W. Zhang, Z.Y. Liu, A. Lutz, F. Zhang, T.L. Zhao, H.C. Ma, X.G. Li, H. Terryn, *Corrosion Science*, 138 (2018) 96.
11. T.G. Wei, R.Q. Zhang, H.Y. Yang, H. Liu, S.Y. Qiu, Y. Wang, P.N. Du, K. He, X.G. Hu, C. Dong, *Corrosion Science*, 158 (2019) 108077.
12. X.Y. San, B. Zhang, B. Wu, X.X. Wei, E.E. Oguzie, X.L. Ma, *Corrosion Science*, 130 (2018) 143.
13. R.P. Earl, F.Z. Victor, *Engineering Fracture Mechanics*, 7 (1975) 371.
14. E. McCafferty, *Corrosion Science*, 47, (2005) 3202.
15. S. P. Qu, X.L. Pang, Y.B. Wang, K.W. Gao, *Corrosion Science*, 75 (2013) 67.
16. J. Soltics, K.A. Lichti, *Corrosion Science*, 68 (2013) 162.
17. A.I. Ikeuba, B. Zhang, J.Q. Wang, E.H. Han, W. Ke, *Journal of Materials Science & Technology*, 35 (2019) 1444.
18. C.H. Paik, H.S. White, R.C. Alkire, *Journal of the electrochemical society*, 147 (2000) 4120.
19. H.Y. Ha, M.H. Jang, T.H. Lee, J. Moon, *Corrosion Science*, 89 (2014) 154.